

Computational Models Predict Larger Muscle Tissue Strains at Faster Sprinting Speeds

NICCOLO M. FIORENTINO¹, MICHAEL R. REHORN², ELIZABETH S. CHUMANOV³, DARRYL G. THELEN^{3,4}, and SILVIA S. BLEMKER^{1,2}

¹Department of Mechanical and Aerospace Engineering, University of Virginia, Charlottesville, VA; ²Department of Biomedical Engineering, University of Virginia, Charlottesville, VA; ³Department of Mechanical Engineering, University of Wisconsin–Madison, Madison, WI; ⁴Department of Biomedical Engineering, University of Wisconsin–Madison, Madison, WI

ABSTRACT

FIORENTINO, N. M., M. R. REHORN, E. S. CHUMANOV, D. G. THELEN, and S. S. BLEMKER. Computational Models Predict Larger Muscle Tissue Strains at Faster Sprinting Speeds. *Med. Sci. Sports Exerc.*, Vol. 46, No. 4, pp. 776–786, 2014. **Introduction:** Proximal biceps femoris musculotendon strain injury has been well established as a common injury among athletes participating in sports that require sprinting near or at maximum speed; however, little is known about the mechanisms that make this muscle tissue more susceptible to injury at faster speeds. **Purpose:** This study aimed to quantify localized tissue strain during sprinting at a range of speeds. **Methods:** Biceps femoris long head (BFLh) musculotendon dimensions of 14 athletes were measured on magnetic resonance (MR) images and used to generate a finite-element computational model. The model was first validated through comparison with previous dynamic MR experiments. After validation, muscle activation and muscle–tendon unit length change were derived from forward dynamic simulations of sprinting at 70%, 85%, and 100% maximum speed and used as input to the computational model simulations. Simulations ran from midswing to foot contact. **Results:** The model predictions of local muscle tissue strain magnitude compared favorably with *in vivo* tissue strain measurements determined from dynamic MR experiments of the BFLh. For simulations of sprinting, local fiber strain was nonuniform at all speeds, with the highest muscle tissue strain where injury is often observed (proximal myotendinous junction). At faster sprinting speeds, increases were observed in fiber strain nonuniformity and peak local fiber strain (0.56, 0.67, and 0.72 for sprinting at 70%, 85%, and 100% maximum speed). A histogram of local fiber strains showed that more of the BFLh reached larger local fiber strains at faster speeds. **Conclusions:** At faster sprinting speeds, peak local fiber strain, fiber strain nonuniformity, and the amount of muscle undergoing larger strains are predicted to increase, likely contributing to the BFLh muscle's higher injury susceptibility at faster speeds. **Key Words:** ACUTE STRAIN INJURY, HAMSTRINGS, ATHLETES, FINITE-ELEMENT MODEL, ACTIVE LENGTHENING

Muscle strain injury remains a prevalent problem in recreational, collegiate, and professional sports, consuming a significant portion of sports medicine practice (24). Athletes participating in high-speed sports, which require sprinting near or at maximum speed, are especially susceptible to acute muscle strain injury (29). Although it has been well documented that the hamstring muscles are highly susceptible to acute injury while sprinting, the amount of local strain experienced by muscle tissue during sprinting and the mechanisms that lead to increased injury risk with speed remain unclear.

Animal models of muscle damage after eccentric contractions have established a strong connection between the magnitude of mechanical strain experienced by muscle and

the extent of damage (28). Furthermore, animal experiments have demonstrated that the site of failure in muscle corresponds to the region of highest localized tissue strain (2). Experiments in animal tissue have also shown directly that muscle is most susceptible to damage when it is actively generating force and lengthening rather than passively lengthening (5,27). *In vivo* experiments during active lengthening in a running guinea fowl found a regionally dependent amount of tissue strain and an increase in local strain with running speed (9). The ideas set forth by animal models of contraction-induced muscle damage provide a strong basis for understanding mechanisms that potentially lead to clinical muscle strain injury; however, the direct application and relation of the results in hamstring muscle mechanics during sprinting at high speeds is relatively limited. One of the goals of the current study was to create computational models of the human hamstrings that allow us to predict localized muscle tissue strain while sprinting at high speeds.

Previous studies of the hamstring muscles during running or sprinting generally acquire external measurements of surface EMG, ground reaction forces, and/or marker-based joint kinematics (40,48). Multiple studies have confirmed that the biceps femoris long head (BFLh) muscle, the most commonly injured hamstring muscle (25), is active and lengthening

Address for correspondence: Silvia S. Blemker, Ph.D., Department of Biomedical Engineering, University of Virginia, 415 Lane Road, Charlottesville, VA 22908; E-mail: ssblemker@virginia.edu.

Submitted for publication March 2013.

Accepted for publication September 2013.

0195-9131/14/4604-0776/0

MEDICINE & SCIENCE IN SPORTS & EXERCISE®

Copyright © 2014 by the American College of Sports Medicine

DOI: 10.1249/MSS.000000000000172

during the late swing phase of sprinting (13,47,50). As sprinting speed increases, previous studies have also shown that the BF muscle activity increases (19), and it does more negative work (i.e., absorbs more energy) (11). Counter to intuition, however, peak musculotendon strain remained invariant at top-end sprinting speeds (11). Although marker-based sprinting studies answer questions about potential injury conditions on the global muscle-tendon unit (MTU) level, injury occurs at the local muscle tissue level; therefore, the behavior of muscle tissue while sprinting may help explain muscle's increased injury susceptibility at faster speeds.

Dynamic imaging and computational modeling have the potential to bridge the gap in knowledge between musculotendon dynamics derived from whole body mechanical models and measurements in animal models of contraction-induced muscle damage. For example, recent advances in dynamic magnetic resonance imaging (MRI) permit strain measurement in muscle tissue during joint motion (52). Dynamic MRI experiments in the BFlh muscle have shown that tissue strain is larger during active compared with passive lengthening (16) and is highest near the BFlh's myotendinous junction (MTJ) (44), which is where injury is frequently observed (1,46). The drawback of dynamic magnetic resonance (MR) experiments is that limitations in scanner bore size and the number of repetitions necessary for dynamic sequences constrain the amount of activation and lengthening that can be studied, which make testing hypotheses about increased strain and higher strain nonuniformity during high-load lengthening contraction infeasible. A recent computational modeling study demonstrated the importance of the BFlh's architecture to its muscle tissue strain distribution and strain injury susceptibility (35); however, the model was not validated against *in vivo* strain measurement, and the simulations were based on non-specific, low levels of activation and muscle-tendon length change. No studies currently exist that show how the behavior of muscle tissue changes with sprinting speed. Understanding how muscle tissue behavior changes with sprinting speed will provide direct insight into muscle's increased injury susceptibility at faster sprinting speeds.

The goals of this study were (i) to generate a finite-element model of the BFlh based on musculotendon dimensions of athletes participating in high-speed sports, (ii) to validate model predictions with *in vivo* dynamic MR experiments, and (iii) to use the model to predict how localized tissue strains in the BFlh are affected by sprinting speed.

METHODS

Finite-element mesh generation and fiber mapping. The dimensions of the finite-element computational mesh were based on the average musculotendon dimensions of the track-and-field athletes of University of Virginia. Fourteen athletes (7 men, height = 177 ± 9 cm, mass = 71 ± 10 kg) provided informed consent to participate in a study approved by the internal review board of the university. All athletes participated in high-speed events and had no

history of acute hamstring strain injury. MR images were acquired with a Siemens Trio 3T MR scanner (Erlangen, Germany) using a Dixon sequence (repetition time = 7 ms, echo time = 2.45 ms, flip angle = 9° , 5-mm slice thickness, field of view = 375×500 mm, imaging matrix = 504×672) with a high spatial resolution (0.74×0.74 mm²). Axial plane images were acquired from the MTU's origin at the hip to the insertion at the knee. The Dixon imaging sequence acquires separately an image when the signal from water and fat is in phase and when the signal from water and fat is out of phase, and the in-phase and out-of-phase images were combined to provide a high contrast between muscle, fat, and connective tissue but not suffer from chemical shift artifact (15).

BFlh musculotendon dimensions were measured directly on MR images using OsiriX Imaging Software (37) (Fig. 1A) or were derived from full segmentations of the muscle using custom in-house MATLAB (The Mathworks, Inc., Natick, MA) software (Table 1). Width and thickness measurements were acquired directly on axial-plane images, whereas muscle length, which runs in the superior–inferior direction perpendicular to the axial imaging plane, was derived from full segmentations. Average musculotendon measurements were used to define the dimensions of the finite-element (FE) mesh, which included three materials (proximal tendon and aponeurosis, muscle, and distal tendon and aponeurosis) connected directly by coincident nodes. A previous modeling study found that a simplified FE computational model based on musculotendon measurements produced the same results as a segmentation-based subject-specific model (35). The FE computational mesh was generated using TrueGrid software (XYZ Scientific Applications) and included 2960 hexahedral elements and 2112 nodes. A convergence study of peak local strain was conducted to determine the number of elements to include in the computational mesh. Representative muscle fibers were mapped through the finite-element mesh from the fibers' origin on the proximal aponeurosis to the fibers' insertion on the distal aponeurosis (4). Muscle fibers were used to define the initial fiber direction at each element, which was an input to the constitutive model, and to calculate spatially varying local tissue strain.

Constitutive model of muscle and connective tissue. A full description of the constitutive model has been published previously (3). Briefly, muscle and connective tissue were modeled as transversely isotropic, hyperelastic, and quasi-incompressible (3,14,49). For a hyperelastic material, stress and strain are related through the following expression:

$$S=2 \times \partial\Phi/\partial C$$

where S is the second Piola–Kirchoff stress tensor, Φ is the strain-energy density function, and C is the right Cauchy–Green strain tensor.

To use transverse isotropy, we defined a preferred direction at each finite element. For tendon, the preferred direction is defined along the length of the connective tissue, or in

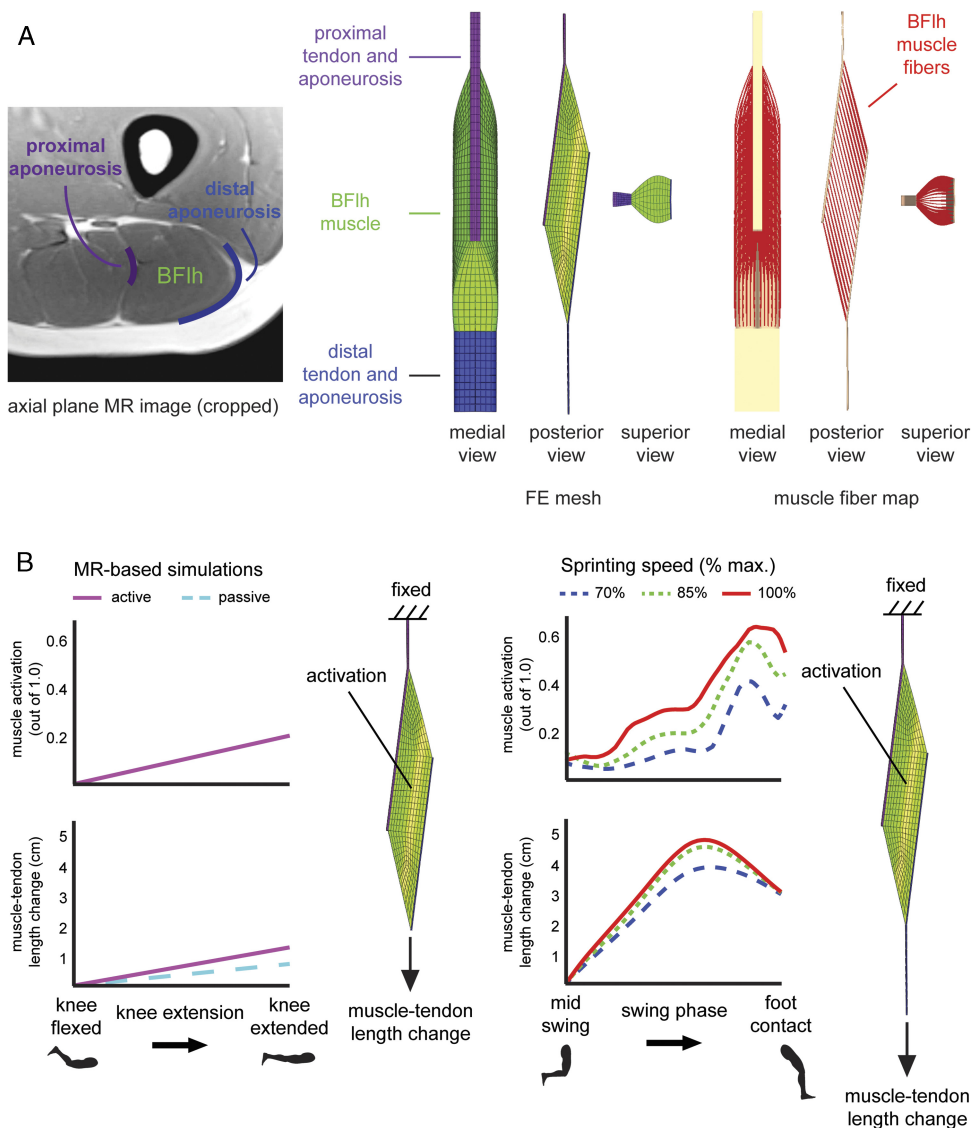


FIGURE 1—Computational model. Musculotendon measurements of collegiate track-and-field athletes were acquired from axial plane MR images and were used to generate a finite-element (FE) computational mesh (A). Muscle fiber direction was defined at each element by mapping fibers through the FE mesh from the fibers’ origin on the proximal aponeurosis to the insertion on the distal aponeurosis (4). To compare model predictions and *in vivo* measurements, we generated a separate computational mesh based on MRI subjects in a previous study (16). The muscle–tendon length change boundary condition was based on the dynamic MR experiment, and muscle activation was based on experiments in the exercise device (45) (B). For sprinting simulations, forward dynamic simulations of measured sprinting kinematics yielded BFLh muscle activation and muscle–tendon length change at 70%, 85%, and 100% of maximum sprinting speed (11). Muscle activation was applied to muscle tissue, and muscle–tendon length change was applied to the distal end of the distal tendon while holding the proximal end fixed. Simulations were performed from midswing to foot contact.

the superior–inferior direction of the element. For muscle, this is defined by the direction of the muscle fiber and specifies the direction along which active stress is generated. The amount of activation linearly modulates muscle fiber’s force–length relationship (51). The amount of stretch in the direction of the fiber is called *along-fiber stretch* (λ). For muscle and connective tissue, the relationship between passive along-fiber stretch and stress is characterized by a nonlinear toe region followed by a linear increase (51). Shear deformation along the fiber and across the fiber are represented by an exponential relationship between shear strain and stress (42). The materials are quasi-incompressible, which is enforced by highly penalizing

changes in volume. Simulations were run with the nonlinear implicit FE solver Nike3D (34). Material constants for muscle (Table 1) were defined based on a recent study of along-fiber extension, cross-fiber extension, and along-fiber shear experiments in muscle tissue (32). Peak isometric stress (i.e., specific tension) was taken from a study on the maximum force-generating capacity of fibers in human vastus lateralis muscle (43). Connective tissue parameters (Table 1) were derived from linear moduli and stress–strain values reported from experiments in tendon (10).

Comparison with dynamic imaging. We previously measured local tissue strains in the BFLh muscle using a dynamic MRI technique (16). The study reported first principal

TABLE 1. Model inputs.

Musculotendon Measurements (cm)																
Muscle				Connective Tissue												
				Proximal Tendon Length	Proximal aponeurosis			Distal aponeurosis			Distal Tendon Length					
AP Width	ML Width	Length	Length		Width	Thickness	Length	Width	Thickness							
4.78 (0.58)	3.93 (0.24)	28.55 (3.78)	5.96 (0.14)	17.32 (1.87)	1.13 (0.24)	0.23 (0.06)	20.89 (1.98)	4.87 (0.55)	0.13 (0.02)	9.61 (1.29)						
Material parameters																
Muscle								Connective tissue								
σ_{max}	P1	P2	λ_{off}	λ^*	A_0	G_c	G_ϕ	K	P1	P2	λ_{off}	λ^*	A_0	G_c	G_ϕ	K
0.125 MPa	0.04	6.6	1.0 Dimensionless	1.06	2.0	3.87×10^{-3} MPa	2.24×10^{-2} MPa	5.0×10^2 MPa	1.2 MPa	50	1.0 Dimensionless	1.03	2.0	3.0 MPa	15.0 MPa	5.0×10^3 MPa

Musculotendon measurements were taken from high-resolution axial plane MR images and averaged across 14 track-and-field athletes of the University of Virginia. Musculotendon measurements were used to define the geometry of the computational mesh. Material parameters were defined for implementation in the transversely isotropic, hyperelastic, and quasi-incompressible material model detailed by Blemker et al. (3). AP, anterior-posterior; ML, medial-lateral; σ_{max} , peak isometric stress; P1, along-fiber extension multiplicative modulus; P2, along-fiber extension exponential modulus; λ_{off} , along-fiber stretch at optimal fiber length; λ^* , stretch at which stress-strain relationship becomes linear; A_0 , exponential shear modulus (42); G_ϕ , along-fiber shear modulus; G_c , cross-fiber shear modulus; K , bulk modulus.

strain in muscle tissue adjacent to the proximal MTJ during passive lengthening and during active lengthening of the BFlh (for $N = 13$ healthy subjects). To compare *in vivo* measurements and model predictions, we generated a separate finite-element computational mesh based on musculotendon dimensions of the subjects in the dynamic imaging study (Fig. 1B). Simulation boundary conditions were defined based on measurements while subjects were exercising in an MR-compatible device that induced lengthening contractions in the hamstrings muscles (45). Because the dynamic MR technique measured displacement in muscle tissue, the muscle-tendon length change boundary condition was applied to the distal MTJ while the proximal end was held fixed. Forward dynamic simulations of subjects exercising in the MR-compatible device were used to define the temporal variation in muscle activation (45,48).

Simulations of sprinting. Muscle activation and musculotendon length change for sprinting were defined based on measured joint kinematics and forward dynamic simulations of sprinting at 70%, 85%, and 100% of maximum speed (Fig. 1B) (11). In a previous study, the forward dynamic simulation framework has been shown to predict similar timing between EMG activity and model predictions for the lateral hamstring muscles (12). A computed muscle control algorithm (48) was used to determine muscle excitation patterns such that the forward dynamic model closely matched joint kinematics measured in 19 athletes during treadmill sprinting (11). To account for muscle redundancy, we used numerical optimization to minimize the sum of squared weighted contractile element forces. Constraints on the timing of muscle excitation were added to ensure that excitations were minimal when EMG data indicated low levels of activation. Muscle-tendon length change and muscle activations were averaged across all subjects. Average activation and length change trajectories at each speed were then applied as boundary conditions to the muscle and the distal end of the computational mesh, respectively. To apply the appropriate amount of MTU length change relative to the length of the MTU, the finite-element simulation began at the muscle-tendon length measured on

MR images, which corresponded to the midswing, or 65% of the gait cycle, and proceeded to foot contact, or 100% of the gait cycle.

Simulation analysis. For each simulation, model predictions of whole muscle fiber length change and local fiber strain were analyzed. To determine whole-fiber length change from simulations, we mapped representative muscle fibers through the computational mesh and tracked throughout the simulation (4). To find local fiber strain, we tracked 61 points along each fiber throughout the finite-element simulation, which permitted values for local fiber strain to be calculated at 60 intrafiber segments along each representative muscle fiber. Local fiber strain was calculated as the difference in intrafiber segment length at each time in the simulation and the original segment length divided by the original length. Local fiber strain is a measure of spatially varying engineering strain. For lengthening, strain is greater than zero. For shortening, strain is less than zero. On the basis of the local fiber strain data, the peak local strain for each fiber was found at each time step in the simulation, and the peak local fiber strain for each fiber was averaged at each sprinting speed. In addition, to assess the amount of strain nonuniformity, peak local fiber strain for each fiber was plotted against the strain of the fiber, where values further away from unity represent more nonuniform strain distributions. Spatially varying fiber strain was analyzed to assess which region(s) of the muscle experienced the largest fiber strain. Fiber strain was averaged in three evenly spaced regions to quantify fiber strain in the muscle tissue near the proximal MTJ, in the middle of the muscle and near the distal MTJ. At the overall peak strain for each speed, a local fiber strain histogram plot demonstrates how much of the muscle was undergoing relatively larger strains.

RESULTS

The model simulation of dynamic MR experiments compared favorably with the experimental measures of tissue strain (Fig. 2). The model predicted first principal strains in

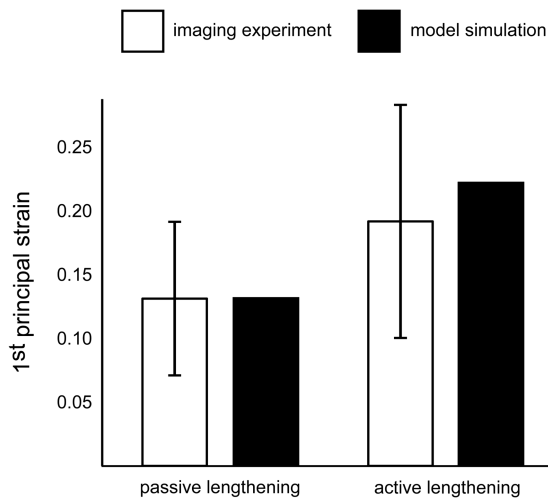


FIGURE 2—Model-imaging comparison. Model simulation results for the first principal strain were compared with *in vivo* measurements in a recent dynamic MRI study (16). Average first principal strain in the muscle tissue adjacent to the proximal MTJ was reported as 0.13 ± 0.06 during passive lengthening experiments and 0.19 ± 0.09 during active lengthening experiments (SD represents variability across $N = 13$ imaging subjects). Model simulation results found an average of 0.13 and 0.22 for passive lengthening and active lengthening, respectively.

muscle tissue adjacent to the proximal MTJ that were within an SD of measurements during both passive lengthening (0.13 vs 0.13 ± 0.06 for MR measurements) and active lengthening (0.22 vs 0.19 ± 0.09 for MR measurements) (SD represents variability across imaging subjects). The similar magnitudes of the first principal strain demonstrate the computational model's ability to replicate muscle tissue strains experienced *in vivo*.

Sprinting simulations showed that whole-fiber length change was nonuniform throughout the BFlh muscle and peaked before foot contact (Fig. 3A). Maximum whole-fiber length change averaged across all representative fibers was 2.7 ± 0.1 , 3.2 ± 0.1 , and 3.3 ± 0.2 cm for maximum MTU lengthening of 3.9, 4.6, and 4.8 cm at maximum sprinting speeds of 70%, 85%, and 100%, respectively. The maximum length change of muscle fibers relative to the length change of the MTU was 0.68, 0.70, and 0.68 at 70%, 85%, and 100% of maximum speed. The strain of the entire MTU was 0.09, 0.10, and 0.11 at 70%, 85%, and 100% of maximum speed. Maximum whole-fiber strain averaged over all fibers was 0.24 ± 0.01 , 0.29 ± 0.01 , and 0.29 ± 0.2 and was at most 0.27, 0.32, and 0.34 for 70%, 85%, and 100% of maximum speed, respectively.

Peak local fiber strain was nonuniform throughout the BFlh muscle, reached a maximum before foot contact, and increased with sprinting speed (Fig. 3B). Averaged over all fibers, peak local fiber strain was 0.46 ± 0.08 , 0.55 ± 0.09 , and 0.59 ± 0.09 , with a maximum of 0.56, 0.67, and 0.72, for sprinting at 70%, 85%, and 100% of maximum speed, respectively. The average peak local fiber strain also increased after normalization by the strain of the MTU (5.20, 5.31, and 5.48 for sprinting at 70%, 85%, and 100% of maximum speed) and was highest at the fastest sprinting speed after

normalization by the average strain of the whole muscle fibers (1.93, 1.91, and 2.01 for sprinting at 70%, 85%, and 100% of maximum speed). Maximum peak local strain also increased with sprinting speed after normalization by MTU strain (6.41, 6.49, and 6.67 for sprinting at 70%, 85%, and 100% of maximum speed) and was highest at the fastest speed after normalization by the maximum whole-fiber strain (2.08, 2.06, and 2.15 for sprinting at 70%, 85%, and 100% of maximum speed).

To assess the uniformity of local fiber strain and the dependency on the strain of the whole fiber, we plotted peak local fiber strain as a function of whole-fiber strain (Fig. 3C). The average distance to the unity line was 0.17 ± 0.05 , 0.20 ± 0.07 , and 0.22 ± 0.06 for sprinting at 70%, 85%, and 100% maximum speed, indicating that local fiber strain becomes more nonuniform with increasing sprinting speed. For comparison, the distance to the unity line was also calculated for simulations of passive and active lengthening MR experiments and was found to be 0.02 ± 0.01 and 0.05 ± 0.01 for passive and active lengthening, respectively.

Fiber strain distribution was found to be nonuniform at each sprinting speed and for MR-based simulations, with the largest fiber strain along the proximal MTJ and decreasing with distance toward the distal MTJ (Fig. 4). Average fiber strain near the proximal MTJ, in the middle of the muscle fibers, and near the distal MTJ increased with sprinting speed, with the largest increases in the muscle tissue near the proximal MTJ. In addition, as sprinting speed increased, a larger portion of the muscle experienced larger local fiber strains, as demonstrated by bigger bins at larger strains in a histogram plot of local fiber strain (Fig. 5).

DISCUSSION

Finite-element model simulations accurately predicted local muscle tissue strains when compared with measurements in dynamic MR experiments, demonstrating the model's ability to predict muscle tissue strains experienced *in vivo*. Simulations of sprinting demonstrated increased BFlh peak local fiber strain and higher fiber strain nonuniformity at faster sprinting speeds. Whole-fiber length change relative to MTU length change remained relatively constant with increasing speed; however, the peak local fiber strain relative to the strain of the MTU increased with speed, and the peak local fiber strain relative to the strain of whole muscle fibers was highest at the fastest speed. These results offer new insights into the deformation of muscle tissue during sprinting and provide a possible explanation for muscle tissue's increased strain injury susceptibility at faster speeds.

This is the first study to provide direct insight into localized muscle tissue strain in the oft-injured hamstring muscles during sprinting because measuring local muscle tissue mechanics while sprinting is not yet possible, and marker-based studies of sprinting gait only provide information

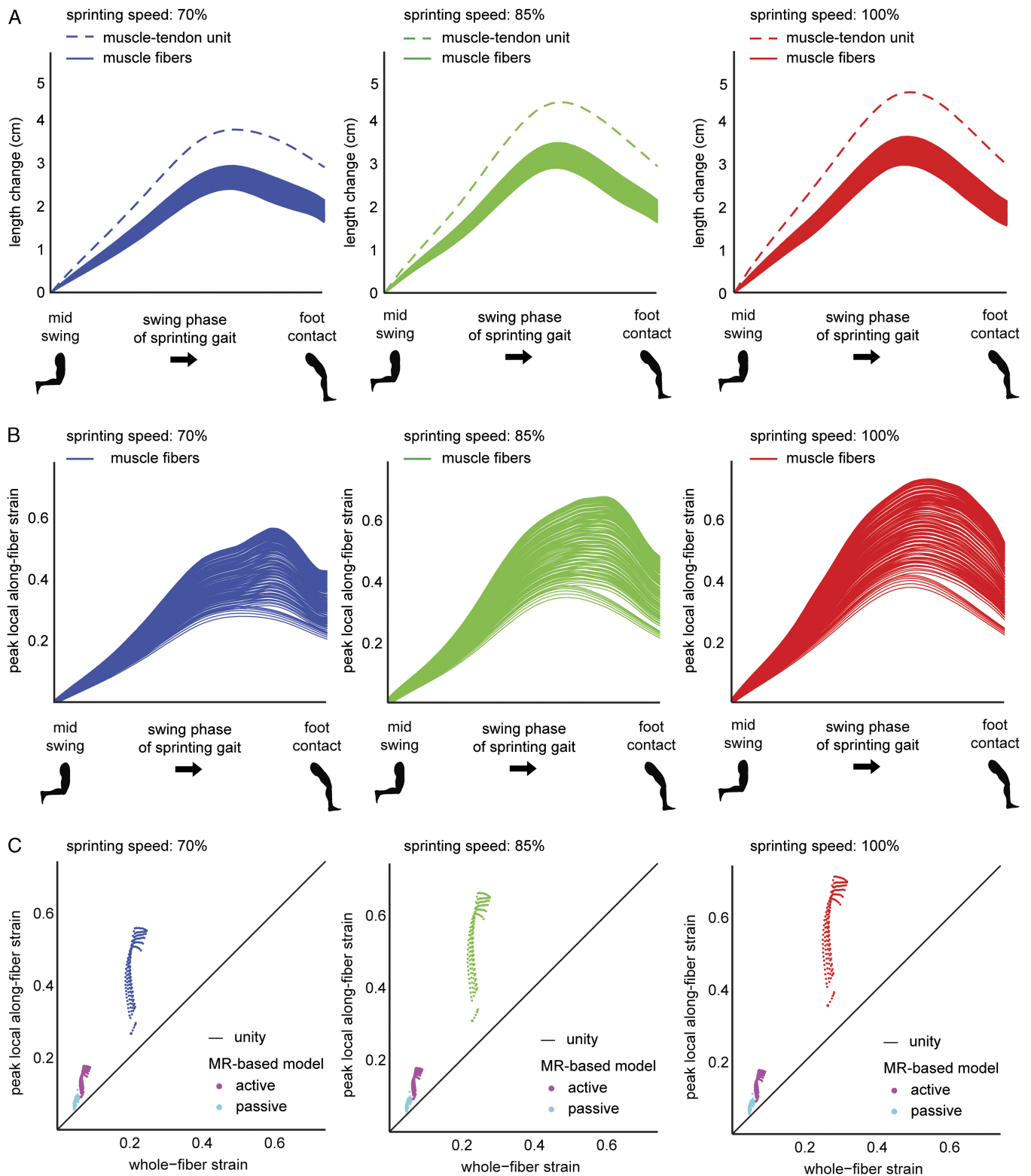


FIGURE 3—Fiber length change, local peak strain, and local peak strain relative to whole-fiber strain. Whole-fiber length change in the FE computational model (muscle fibers) was nonuniform throughout the BFlh muscle and increased with sprinting speed (A) (representative fibers are plotted as individual lines). The boundary condition for MTU length change was plotted for comparison (MTU). Peak local along-fiber strain was found for each representative muscle fiber (B). To assess the uniformity of fiber strain while sprinting and during dynamic MR experiments, we plotted local peak fiber strain as a function of whole-fiber strain for each representative fiber (C). Values on the unity line represent perfectly uniform strain distribution along the fiber.

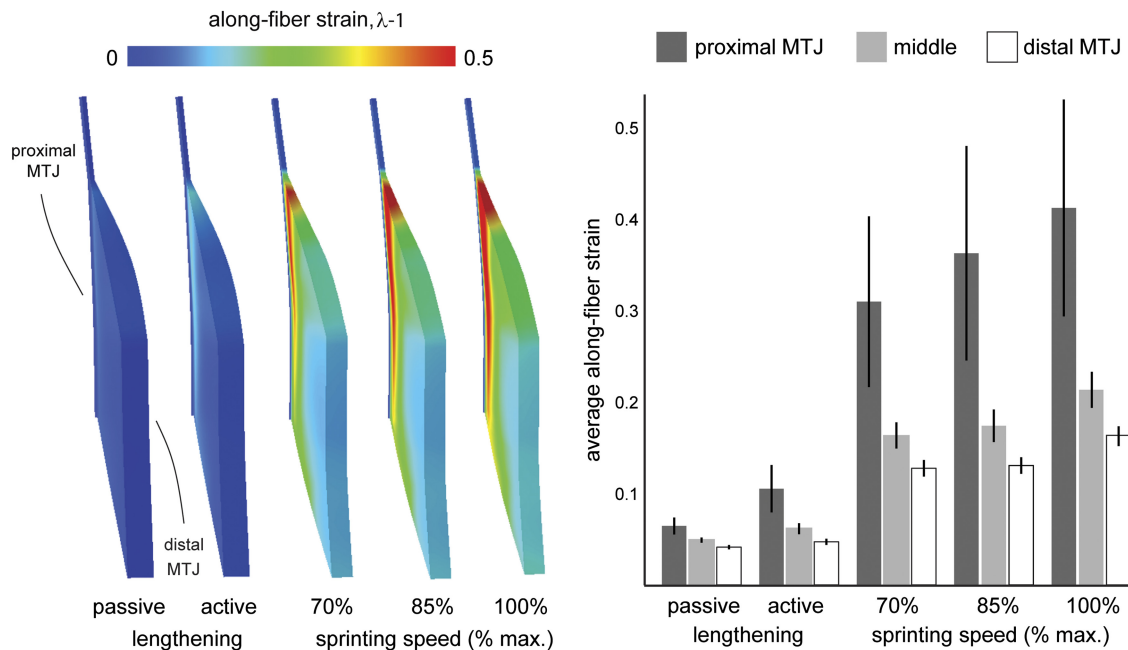


FIGURE 4—Along-fiber strain distribution. Along-fiber strain distribution was analyzed at the time of maximum local strain and was found to be nonuniform throughout the BFLh muscle (shown in longitudinal cross section). Color maps of along-fiber strain distribution are shown for simulations of passive and active lengthening during dynamic MR experiments and for sprinting at 70%, 85%, and 100% of maximum speed. Along-fiber strain was averaged in three evenly spaced regions along the muscle fibers from the proximal MTJ to the distal MTJ. Average along-fiber strain was found to decrease as a function of distance from the proximal MTJ at each speed and to increase as a function of speed in each region.

about the behavior of the entire MTU. In the current study, we combined forward dynamic simulation output with finite-element modeling to study the effect of increased sprinting speed on local muscle fiber strain. Previous forward dynamic simulations of sprinting matched marker measurements of joint kinematics by driving a lumped parameter muscle–tendon model with activations (48), or an inverse dynamics approach has been used along with static optimization to derive MTU results from calculated joint torques (40). Marker-based studies of sprinting have shown that the BFLh MTU does more work with increasing sprinting speed (11,39); however, insights into the behavior of the MTU only provide a more global mechanism for muscle injury. The power of the modeling approach described in this paper is that the output of the computational model is spatially varying tissue strain, which can identify regions of large localized tissue strain and test hypotheses about what factors lead to increases in strain injury susceptibility.

At all speeds, the computational model found that local fiber strain was nonuniform throughout the BFLh muscle and highest along the proximal MTJ (Fig. 4), which corresponds to the most frequent injury location in the BFLh (1,46). Large localized fiber strain where injury is frequently observed supports the hypothesis that large localized tissue strain is the injury mechanism in lengthening contractions during sprinting. Experimental studies in humans have also measured regionally varying muscle tissue strain (52) and higher strain closer to the proximal MTJ in the BFLh during lengthening contractions (44). In all three evenly spaced regions along the

muscle fiber, sprinting simulations showed that the average magnitude of fiber strain increased with increasing speed, with the largest increases in the muscle tissue near the proximal MTJ. These results are in agreement with sonomicrometry experiments in guinea fowl that found local tissue strain increased with running speed, and increases were the largest in regions that experienced the largest strains at slower speeds (9). The current study's results are the first to demonstrate increased muscle tissue strain with sprinting speed in humans, which is important because the BFLh's increased injury susceptibility with sprinting speed has yet to be explained on the local muscle tissue level.

Model simulations found that peak local fiber strain was nonuniform throughout the BFLh and occurred during the late swing phase of sprinting (before foot contact) (Fig. 3B), which corresponds well with the timing of acute strain injury observed during sprinting kinematics studies (18,38). The amount of strain nonuniformity increased with sprinting speed, as shown by the larger in difference normalized peak local fiber strain and whole-fiber strain in Figure 3C (0.17, 0.20, and 0.22 for sprinting at 70%, 85%, and 100% maximum speed). Furthermore, as sprinting speed increased, more of the muscle experienced higher fiber strain, which is shown by the relatively larger bins at larger fiber strains in the histogram in Figure 5. If acute muscle strain injury is sustained by tissue strain crossing an injury threshold, as suggested by injury after single active stretches in animal experiments (17), more of the muscle will be susceptible to injury at faster speeds. Similarly, if muscle injury occurs after the accumulation of damage to muscle tissue during an

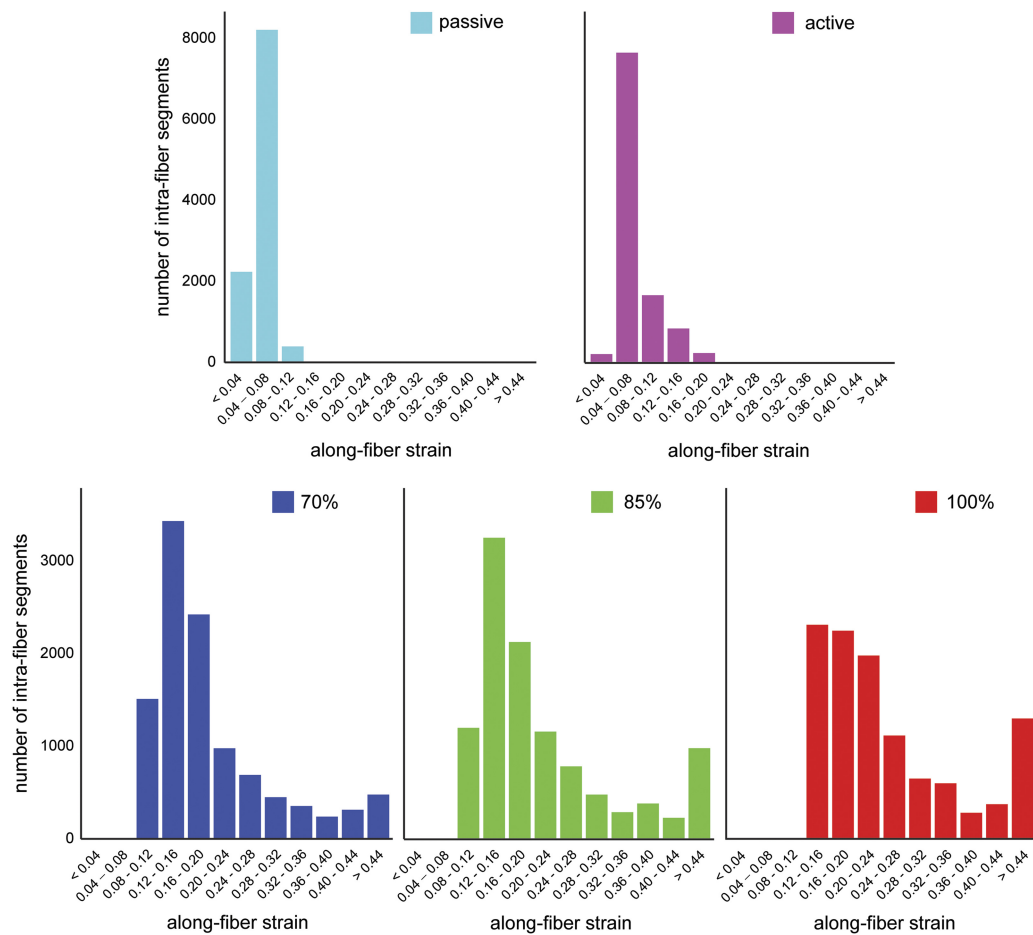


FIGURE 5—Histogram of along-fiber strain. Local along-fiber strain was calculated for 60 intrafiber segments along 180 fibers and was binned according to amount of strain. Histograms are shown for simulations of passive and active lengthening during dynamic MR experiments (*top row*) and for sprinting at 70%, 85%, and 100% of maximum speed (*bottom row*). Bigger bins to the right indicate a higher portion of the muscle undergoing larger strains.

activity, as suggested by stretch–shortening cycles in animals over physiological ranges (8), more muscle tissue undergoing larger tissue strain will increase muscle’s strain injury susceptibility at faster sprinting speeds.

The observed increase in strain nonuniformity and peak local strain was a result of higher muscle activations at faster speeds. The primary factor that leads to this phenomenon is the converging of the BFlh’s longitudinal cross-sectional area near the proximal MTJ. The region of the muscle tissue near the proximal MTJ is smaller in the cross-sectional area than that in the neighboring regions in the middle of the muscle and near the distal MTJ. The relatively larger cross-sectional areas of adjacent tissue generate more force for a given amount of muscle activation, and the larger forces must be balanced by forces generated in tissue near the proximal MTJ. Given the smaller cross-sectional area, the muscle tissue near the proximal MTJ will experience higher stresses and as a result undergo greater strain than neighboring tissue. Higher levels of activation at faster sprinting speeds will exacerbate this effect because of the muscle’s nonlinear force–length relationship, and tissue near the proximal MTJ will strain even more. More specifically, at

higher activation levels, the active force–length curve will influence the total force–length curve more, and given that strains in these simulations occur on the descending limb of the force curve, relatively more strain will be necessary for a given increase in stress.

Animal experiments are able to relate directly the amount of strain and damage to muscle tissue. A study in rabbit extensor digitorum longus MTU found that an active strain of 0.15 (of the entire MTU) was necessary to detect damage (17), although the threshold for muscle damage from imposed strain has not been consistent in the literature. Other studies found that much higher amounts of active MTU strain are necessary to produce damage (e.g., 0.30 strain in Brooks et al. [5]). Both thresholds are larger than the amount of MTU strain in this study (0.11 for sprinting at 100% maximum speed). On the local level, a previous study measured local mechanical strain during passive extension of animal MTU, and muscle tissue was shown to suffer damage at a local mechanical strain of 0.61 (2). The maximum peak local strain in the current modeling study was 0.72 at 100% maximum sprinting speed. It should be noted that the reference configuration for the current study is midswing, which is not passively unloaded

like animal MTU studies, and therefore, caution should be taken when directly comparing the results of the current modeling study to those of animal studies.

The relative amount of muscle fiber strain to MTU strain in sprinting simulations was slightly larger than observations in active lengthening of intact rabbit MTUs. Sprinting simulations had 2.7 times more fiber strain than MTU strain for 100% maximum speed, and rabbit MTU lengthening experiments showed approximately 2.6 times more fiber strain than MTU strain averaged over the course of many strain shorten cycles (7). As demonstrated by the same study, the relative amount of muscle fiber strain in animal MTU experiments depends on the reference length (7). In addition, the muscle–tendon architecture, the magnitude of length change, and the amount of activation will alter the amount of muscle fiber strain relative to MTU strain. It would also be expected that, relative to the submaximal activations in the current study, maximally activated muscle in animal studies will generate more force and cause more tendon stretch for a given MTU lengthening and result in relatively less muscle fiber strain. In any case, the results presented here demonstrate that the magnitude of MTU strain (0.11) is not representative of the amount of muscle fiber strain (0.29 ± 0.02 for sprinting at 100% maximum), which is also not representative of the amount of local fiber strain (peak = 0.59 ± 0.09 for sprinting at 100% maximum speed).

Although the magnitudes differed, the shape of the curves for MTU length change, whole-fiber length change, and peak local along-fiber strain was qualitatively similar with only a shift of peak local along-fiber strain relative to MTU and whole-fiber length change (Figs. 3A and 3B). The shift was speed dependent, with maximum local along-fiber strain occurring slightly later for faster speeds, suggesting that the timing between activation and MTU length could have an effect on the timing of peak local strain. Sonomicrometry experiments in animals (6,30,36) and ultrasound experiments in humans (21) have observed a much larger timing difference between MTU and fiber dynamics. These experiments, however, were performed during different tasks, on different muscles, and with different relative timings between muscle activation and MTU length change. Moreover, the shape of the MTU length change and activation curves likely differed from the current study, making a direct comparison between studies more difficult.

The computational model's material parameters incorporated recent measurements in muscle (32) and connective tissue (10). A sensitivity analysis of material parameters showed that the shear properties of tendon had the least effect on muscle fiber strain and peak local tissue strain, with twice as stiff and twice as compliant tendon shear moduli resulting in a less than 1% change in peak local fiber strain. On the other hand, doubling the along-fiber stiffness of tendon had a larger influence on muscle tissue strain, with twice as stiff along-fiber extension moduli (P1 and P2), yielding an 11% increase in peak along-fiber strain. The dependence of muscle fiber strain on tendon stiffness has also been observed in forward dynamic simulations of

running (47). It should be noted that the choice of material model affects the strain magnitude and distribution of model predictions. Specifically, the anisotropy of intramuscular tissues can introduce anisotropy in the transverse direction (41), which has been suggested in a previous two-dimensional modeling study of a pennate MTU to influence strain (20). With respect to the current study's results, introducing transverse anisotropy would likely not influence our conclusions because our sensitivity analysis had varied along-fiber shear modulus—which would be affected directly by inducing transverse anisotropy—and the strain distribution and magnitude was not changed.

Of all the parameters, peak isometric stress had the biggest influence on peak local fiber strain, with a 50% increase in peak isometric stress resulting in an increase of 13% in peak along-fiber strain. It should be noted that peak isometric stress is an intrinsic property of muscle fibers that may not necessarily change with training. Training likely alters neuromuscular coordination (i.e., the magnitude and timing of muscle activation and muscle–tendon length change) and the amount of muscle tissue available for generating force (i.e., muscle hypertrophy) rather than muscle's intrinsic ability to generate force. Muscle's intrinsic ability to generate force could be changed by altering fiber type composition, given that different fiber types exhibit different levels of peak isometric stress (43). Although the model's results were sensitive to perturbations in certain material parameters, the values that were used yielded results that match experimental data, which inspires confidence in the model's ability to replicate tissue strains experienced *in vivo*. Furthermore, the conclusions of this study regarding increases in tissue strain at faster sprinting speeds were not altered by changes in the model's material parameters.

The current study's model results help fill the gap in knowledge between whole-body kinematics studies and animal muscle fiber experiments by predicting local fiber strain during physiological muscle activations and muscle–tendon length changes. This approach can be used in future studies of tissue-level muscle function during movements that cannot be imaged directly or measured with joint-level kinematic studies. A future application of this modeling framework would be to generate finite-element models based on the range of musculotendon dimensions rather than using one mesh of the average dimensions of all subjects, as previous modeling study (35) and imaging experiments (16,44) have found a connection between musculotendon morphology and internal muscle tissue strains. In addition, an anatomical study has found variable thickness of the BFlh muscle along its length (23), which could influence strain experienced by muscle. However, a previous modeling study that included variable muscle thickness simulated active lengthening of the BFlh and found a similar strain distribution as the current study (35). In the present study, our goal was to address the effects of increased running speed and not the influence of subject musculotendon dimensions. An additional consideration in future studies would be to

collect dynamic MR images, musculotendon dimensions, motion capture, and EMG data on the same subjects rather than incorporate data from different sources like in the current study. This approach would also permit further validation of the modeling approach, where subject-specific FE model simulations with individualized boundary conditions could be performed for each subject and validated against subject-specific strain measurements.

In addition, the reference configuration for the current study was in the middle of the swing phase of sprinting because the muscle-tendon length measured on MR images corresponded to the MTU length at 65% of the sprinting gait cycle in forward dynamic simulations; future simulations starting from an earlier point in the gait cycle might find a different absolute magnitude of fiber strain and relative change with speed. Moreover, similar changes might accompany simulations that continue until later points in the gait cycle, such as through the stance phase, where high amounts of BFlh activation have been measured (22,26,31), and it has been suggested as a time when the hamstring muscles may be vulnerable to injury (33). Future simulation efforts should also investigate a wider range of speeds to further elucidate the connection between muscle tissue strain and sprinting speed, as a couple of normalized values (average peak local fiber strain normalized by average strain of whole muscle fibers and maximum peak local strain normalized by maximum whole-fiber strain) were lower at 85% than 70% (although all values were highest at 100% maximum speed).

An additional limitation to the current approach is that the effects of contraction velocity and passive viscoelasticity were not included in the constitutive formulation. Future model developments include adding these effects in the constitutive equation, which will possibly alter changes with speed, including the relative magnitude strain and the timing between activation, MTU lengthening, and local fiber strain. Lastly, the displacement boundary condition for the simulations in this study was applied to the distal end while holding the proximal end fixed, which was based on the length change output from forward dynamic simulations. Applying separate length changes to the MTU at the knee and hip to incorporate simultaneous joint angle changes would result in the same strain distributions because the computational model does not take into account inertial

effects and the MTU is not mechanically coupled with neighboring muscles.

To summarize, we developed a unique approach to reveal the tissue-level behavior of the oft-injured BFlh muscle during sprinting. Forward dynamic simulation output of muscle activation and muscle-tendon length change were incorporated into a finite-element model of sprinting at faster speeds. The models showed that as sprinting speed increases, so does peak local fiber strain, fiber strain non-uniformity, and the amount of muscle tissue that undergoes larger strain. Increases in peak local fiber strain are attributed to the converging of the BFlh cross-sectional area near the proximal MTJ and increases in muscle activation at faster sprinting speed. Increased peak local fiber strain in the muscle tissue where injury is often found provides additional evidence for the hypothesis that localized fiber strain is the injury mechanism during lengthening contractions. Larger peak fiber strain, higher fiber strain nonuniformity, and higher percentage of the muscle undergoing larger strain provide evidence that may explain muscle's increased strain injury susceptibility at faster sprinting speeds and in high-speed sports.

With the current modeling approach, future model simulations can aid in the design and vetting of potential neuromuscular coordination strategies for reducing strain injury incidence by testing which strategies reduce localized muscle tissue strain. Furthermore, with a better understanding of the connection between neuromuscular strategies and increased strain injury susceptibility at faster sprinting speeds, future training programs can be designed to limit the variables that lead to increased injury susceptibility and reduce the number of acute muscle strain injuries.

This work was supported by the National Institutes of Health (grant no. R01 AR056201). The authors also thank the Achievement Rewards for College Scientists Foundation for their support. They thank Amy Silder and Christopher Westphal for their assistance with dynamic MRI testing and forward dynamic simulations of MR experiments. They also thank Natalie Kramer and Christopher Herb for their assistance in recruiting track-and-field athletes at the University of Virginia.

The authors have no conflicts of interest to disclose.

The results of the present study do not constitute endorsement by the American College of Sports Medicine.

REFERENCES

1. Askling CM, Tengvar M, Saartok T, Thorstensson A. Acute first-time hamstring strains during high-speed running: a longitudinal study including clinical and magnetic resonance imaging findings. *Am J Sports Med.* 2007;35(2):197–206.
2. Best T, McElhaney J, Garrett W, Myers B. Axial strain measurements in skeletal muscle at various strain rates. *J Biomech Eng.* 1995;117(3):262–5.
3. Blemker SS, Pinsky PM, Delp SL. A 3D model of muscle reveals the causes of nonuniform strains in the biceps brachii. *J Biomech.* 2005;38(4):657–65.
4. Blemker SS, Delp SL. Three-dimensional representation of complex muscle architectures and geometries. *Ann Biomed Eng.* 2005;33(5):661–73.
5. Brooks SV, Zerba E, Faulkner JA. Injury to muscle fibers after single stretches of passive and maximally stimulated muscles in mice. *J Physiol.* 1995;488(2):459–69.
6. Butterfield TA, Herzog W. Effect of altering starting length and activation timing of muscle on fiber strain and muscle damage. *J Appl Physiol.* 2006;100(5):1489–98.
7. Butterfield TA, Herzog W. Quantification of muscle fiber strain during in vivo repetitive stretch-shortening cycles. *J Appl Physiol.* 2005;99(2):593–602.
8. Butterfield TA. Eccentric exercise in vivo: strain-induced muscle damage and adaptation in a stable system. *Exerc Sport Sci Rev.* 2010;38(2):51–60.

9. Carr JA, Ellerby DJ, Marsh RL. Differential segmental strain during active lengthening in a large biarticular thigh muscle during running. *J Exp Biol*. 2011;214(20):3386–95.
10. Chandrashekar N, Slaughterbeck J, Hashemi J. Effects of cyclic loading on the tensile properties of human patellar tendon. *Knee*. 2012;19(1):65–8.
11. Chumanov ES, Heiderscheid BC, Thelen DG. The effect of speed and influence of individual muscles on hamstring mechanics during the swing phase of sprinting. *J Biomech*. 2007;40(16):3555–62.
12. Chumanov ES, Heiderscheid BC, Thelen DG. Hamstring musculotendon dynamics during stance and swing phases of high-speed running. *Med Sci Sports Exerc*. 2011;43(3):525–32.
13. Chumanov ES, Schache AG, Heiderscheid BC, Thelen DG. Hamstrings are most susceptible to injury during the late swing phase of sprinting. *Br J Sports Med*. 2012;46(2):90.
14. Criscione JC, Douglas AS, Hunter WC. Physically based strain invariant set for materials exhibiting transversely isotropic behavior. *J Mech Phys Solids*. 2001;49(4):871–97.
15. Dixon W. Simple proton spectroscopic imaging. *Radiology*. 1984;153(1):189–94.
16. Fiorentino NM, Epstein FH, Blemker SS. Activation and aponeurosis morphology affect in vivo muscle tissue strains near the myotendinous junction. *J Biomech*. 2012;45(4):647–52.
17. Hasselman CT, Best TM, Seaber AV, Garrett WE. A threshold and continuum of injury during active stretch of rabbit skeletal muscle. *Am J Sports Med*. 1995;23(1):65–73.
18. Heiderscheid BC, Hoerth DM, Chumanov ES, Swanson SC, Thelen BJ, Thelen DG. Identifying the time of occurrence of a hamstring strain injury during treadmill running: a case study. *Clin Biomech (Bristol, Avon)*. 2005;20(10):1072–8.
19. Higashihara A, Ono T, Kubota J, Okuwaki T, Fukubayashi T. Functional differences in the activity of the hamstring muscles with increasing running speed. *J Sports Sci*. 2010;28(10):1085–92.
20. Hodgson JA, Chi S, Yang JP, Chen J, Edgerton VR, Sinha S. Finite element modeling of passive material influence on the deformation and force output of skeletal muscle. *J Mech Behav Biomed Mater*. 2012;9:163–83.
21. Ishikawa M, Pakaslahti J, Komi PV. Medial gastrocnemius muscle behavior during human running and walking. *Gait Posture*. 2007;25(3):380–4.
22. Jonhagen S, Ericson M, Nemeth G, Eriksson E. Amplitude and timing of electromyographic activity during sprinting. *Scand J Med Sci Sports*. 1996;6(1):15–21.
23. Kellis E, Galanis N, Natsis K, Kapetanios G. Muscle architecture variations along the human semitendinosus and biceps femoris (long head) length. *J Electromyogr Kinesiol*. 2010;20(6):1237–43.
24. Kibler WB. Clinical aspects of muscle injury. *Med Sci Sports Exerc*. 1990;22(4):450–2.
25. Koulouris G, Connell D. Evaluation of the hamstring muscle complex following acute injury. *Skeletal Radiol*. 2003;32(10):582–9.
26. Kyrolainen H, Avela J, Komi P. Changes in muscle activity with increasing running speed. *J Sports Sci*. 2005;23(10):1101–9.
27. Lieber RL, Woodburn TM, Friden J. Muscle damage induced by eccentric contractions of 25% strain. *J Appl Physiol*. 1991;70(6):2498–507.
28. Lieber RL, Friden J. Muscle damage is not a function of muscle force but active muscle strain. *J Appl Physiol*. 1993;74(2):520–6.
29. Lysholm J, Wiklander J. Injuries in runners. *Am J Sports Med*. 1987;15(2):168–71.
30. Maas H, Gregor RJ, Hodson-Tole EF, Farrell BJ, Prilutsky BI. Distinct muscle fascicle length changes in feline medial gastrocnemius and soleus muscles during slope walking. *J Appl Physiol*. 2009;106(4):1169–80.
31. Mero A, Komi PV. Electromyographic activity in sprinting at speeds ranging from sub-maximal to supra-maximal. *Med Sci Sports Exerc*. 1987;19(3):266–74.
32. Morrow DA, Donahue TLH, Odegard GM, Kaufman KR. Transversely isotropic tensile material properties of skeletal muscle tissue. *J Mech Behav Biomed Mater*. 2010;3(1):124–9.
33. Orchard JW. Hamstrings are most susceptible to injury during the early stance phase of sprinting. *Br J Sports Med*. 2012;46(2):88–9.
34. Puso MA, Maker BN, Ferencz RM, Hallquist JO. NIKE3D: a nonlinear, implicit, three-dimensional finite element code for solid and structural mechanics. User's manual. Report UCRL-MA-105268. Lawrence Livermore National Laboratory; 2007.
35. Rehorn MR, Blemker SS. The effects of aponeurosis geometry on strain injury susceptibility explored with a 3D muscle model. *J Biomech*. 2010;43(13):2574–81.
36. Roberts TJ, Azizi E. The series-elastic shock absorber: tendons attenuate muscle power during eccentric actions. *J Appl Physiol*. 2010;109(2):396–404.
37. Rosset A, Spadola L, Ratib O. OsiriX: an open-source software for navigating in multidimensional DICOM images. *J Digital Imaging*. 2004;17(3):205–16.
38. Schache AG, Wrigley TV, Baker R, Pandy MG. Biomechanical response to hamstring muscle strain injury. *Gait Posture*. 2009;29(2):332–8.
39. Schache AG, Blanch PD, Dorn TW, Brown NAT, Rosemond D, Pandy MG. Effect of running speed on lower limb joint kinetics. *Med Sci Sports Exerc*. 2011;43(7):1260–71.
40. Schache AG, Dorn TW, Blanch PD, Brown NAT, Pandy MG. Mechanics of the human hamstring muscles during sprinting. *Med Sci Sports Exerc*. 2012;44(4):647–58.
41. Sharafi B, Blemker SS. A micromechanical model of skeletal muscle to explore the effects of fiber and fascicle geometry. *J Biomech*. 2010;43(16):3207–13.
42. Sharafi B, Ames EG, Holmes JW, Blemker SS. Strains at the myotendinous junction predicted by a micromechanical model. *J Biomech*. 2011;44(16):2795–801.
43. Shoepe TC, Stelzer JE, Garner DP, Widrick JJ. Functional adaptability of muscle fibers to long-term resistance exercise. *Med Sci Sports Exerc*. 2003;35(6):944–51.
44. Silder A, Reeder SB, Thelen DG. The influence of prior hamstring injury on lengthening muscle tissue mechanics. *J Biomech*. 2010;43(12):2254–60.
45. Silder A, Westphal CJ, Thelen DG. A magnetic resonance-compatible loading device for dynamically imaging shortening and lengthening muscle contraction mechanics. *J Med Devices*. 2009;3(3):1–5.
46. Silder A, Heiderscheid BC, Thelen DG, Enright T, Tuite MJ. MR observations of long-term musculotendon remodeling following a hamstring strain injury. *Skeletal Radiol*. 2008;37(12):1101–9.
47. Thelen DG, Chumanov ES, Best TM, Swanson SC, Heiderscheid BC. Simulation of biceps femoris musculotendon mechanics during the swing phase of sprinting. *Med Sci Sports Exerc*. 2005;37(11):1931–8.
48. Thelen DG, Anderson FC. Using computed muscle control to generate forward dynamic simulations of human walking from experimental data. *J Biomech*. 2006;39(6):1107–15.
49. Weiss JA, Maker BN, Govindjee S. Finite element implementation of incompressible, transversely isotropic hyperelasticity. *Comput Methods Appl Mech Eng*. 1996;135(1-2):107–28.
50. Yu B, Queen RM, Abbey AN, Liu Y, Moorman CT, Garrett WE. Hamstring muscle kinematics and activation during overground sprinting. *J Biomech*. 2008;41(15):3121–6.
51. Zajac FE. Muscle and tendon: properties, models, scaling, and application to biomechanics and motor control. *Crit Rev Biomed Eng*. 1989;17:359–411.
52. Zhong X, Epstein FH, Spottiswoode BS, Helm PA, Blemker SS. Imaging two-dimensional displacements and strains in skeletal muscle during joint motion by cine DENSE MR. *J Biomech*. 2008;41(3):532–40.